International Journal of Offshore and Polar Engineering (ISSN 1053-5381)

Vol. 36, No. 2, June 2026, pp. 172–179; https://doi.org/10.17736/ijope.2026.sq01

http://www.isope.org/publications

Super-Resolution Reconstruction of Near-Wall Turbulence Based on SRCNN and U-Net Frameworks

Guoqing Fan
Computational Marine Hydrodynamics Lab (CMHL)
School of Naval Architecture, Ocean and Civil Engineering, Shanghai Jiao Tong University, Shanghai, China

Hanqiao Han
Wuhan Second Ship Design and Research Institute
Wuhan, China

Guibin Chen
Zhongnan Engineering Corporation Limited
Changsha, China

Decheng Wan*†
Computational Marine Hydrodynamics Lab (CMHL)
School of Naval Architecture, Ocean and Civil Engineering, Shanghai Jiao Tong University, Shanghai, China

In this study, super-resolution reconstruction of near-wall turbulence is conducted using two deep neural networks: a conventional super-resolution convolutional neural network (SRCNN) and a U-Net-based super-resolution architecture (U-NetSR). The training data are derived from high-fidelity, wall-resolved large eddy simulations of turbulent channel flow at $Re_\tau = 1{,}000$, while low-resolution inputs are generated by downsampling with ratios $r = 4$ and $r = 8$. We focus specially on the reconstruction performance in different regions of the turbulent boundary layer: the inner layer ($y^+ = 15$) and the outer layer ($y/\delta = 0.15$). The results demonstrate that both methods significantly outperform bicubic interpolation, with U-NetSR showing superior reconstruction accuracy across all test cases. At higher downsampling ratios ($r = 8$), SRCNN tends to oversmooth the flow field, whereas U-NetSR preserves small-scale structures and high-frequency features more effectively. Moreover, the reconstruction performance is consistently better in the outer layer than in the inner layer, due to the richer and more complex flow details present near the wall. These findings highlight the potential of deep learning-based models, particularly the U-Net architecture, in enhancing the resolution of turbulent fields while reducing computational cost.

INTRODUCTION

For high Reynolds number wall-bounded turbulence, accurately resolving near-wall coherent structures and capturing small-scale motions requires substantial computational resources, which in turn makes obtaining high-resolution (HR) data exceedingly challenging. In practical marine environments, high-fidelity simulations (such as direct numerical simulation, DNS) or measurements of turbulent flows around ship hulls, offshore platforms, and subsea structures are often limited by spatial resolution and computational resources. In this context, super-resolution (SR) reconstruction methods offer a novel perspective by reconstructing HR flow fields from low-resolution (LR) inputs. SR methods provide a promising direction for alleviating computational challenges and enhancing the accessibility of high-fidelity flow data, thus opening new avenues for turbulence research and engineering applications.

* ISOPE Member; † Corresponding author.

Received July 26, 2025; updated and further revised manuscript received by the editors November 20, 2025. The original version (prior to the final updated and revised manuscript) was presented at the Thirty-fifth International Ocean and Polar Engineering Conference (ISOPE-2025), Goyang/Seoul, Korea, June 1–6, 2025.

KEY WORDS: Super-resolution reconstruction, wall-bounded turbulence, large-eddy simulation, U-Net framework.

The concept of super-resolution convolutional neural networks (SRCNN) was first introduced by Dong et al. (2016) in their seminal work. This pioneering study demonstrated the capability of deep learning models to reconstruct HR images from LR inputs, marking a significant milestone in the field of image processing. Since its inception, SRCNN and its extensions have been widely adopted in various scientific and engineering domains, including fluid mechanics and turbulence modeling. In the context of near-wall turbulence, recent studies have explored the application of SRCNN-based methods to reconstruct small-scale flow features from coarse-grained simulation or experimental data. The pioneering work by Fukami et al. (2019) introduced machine-learning (ML) based SR methods, utilizing CNN and hybrid downsampled skip- connection/multi-scale models. These methods demonstrated the ability to reconstruct HR turbulent fields, such as two-dimensional cylinder wake and homogeneous isotropic turbulence, from coarse input data with remarkable accuracy. Subsequently, Fukami et al. (2021) extended this approach to spatiotemporal SR reconstruction, integrating temporal dynamics to enhance predictive accuracy in turbulent channel flows. Recent advancements have incorporated novel architectures to further improve reconstruction capabilities. Zhou et al. (2022) presented a 3D-CNN-based turbulence volumetric super-resolution (TVSR) model that, when trained on low-Reynolds-number DNS data, accurately reconstructs high-resolution isotropic turbulence from low-resolution LES and filtered DNS across a wide Reynolds-number range. Xu et al. (2023) proposed a transformer-based SR model, leveraging its superior ability to capture long-range dependencies and multiscale features, enabling high-quality reconstruction of isotropic and anisotropic turbulent properties. Similarly, Zeng et al. (2024) developed a hybrid attention framework that effectively integrates multi-dimensional feature fusion, demonstrating its efficacy in reconstructing both laminar and turbulent flows from LR datasets.

In addition to the aforementioned SRCNN-based studies, another major class of SR methods is based on the generative adversarial network (GAN). Deng et al. (2019) pioneered the use of SRGAN and enhanced-SRGAN (ESRGAN) to super-resolve turbulent velocity fields from PIV data with high fidelity, robust statistical recovery, and strong generalization to complex wake flows. Kim et al. (2021) introduced an unsupervised cycleGAN that reconstructs DNS-quality turbulence from unpaired LES data, demonstrating robust statistical fidelity and cross-Reynolds-number generalization. Nista et al. (2024) systematically compared a SRGAN with its supervised CNN counterpart for turbulent SR and concluded that the discriminator-mediated adversarial training yields significantly higher accuracy in reconstructing sub-filter-scale gradients and intermittency while enabling robust extrapolation to unseen filter kernels, upsampling ratios, and higher Reynolds numbers. Wu et al. (2024) introduced the energy-cascade SRGAN framework with physics-embedded losses and trained solely on channel-flow DNS, enabling zero-shot, multi-ratio reconstruction of small-scale wall-turbulence structures with DNS-level fidelity across diverse TBL datasets.

While CNN- and GAN-based methods have demonstrated impressive performance in super-resolving turbulent flow fields, their capacity to recover small-scale near-wall structures—particularly in wall-bounded turbulence—remains constrained by architectural limitations. Notably, standard CNNs may struggle to capture multi-scale features effectively, while GANs often suffer from training instability and mode collapse, especially in complex, high-dimensional turbulent systems. To address these challenges, encoder-decoder architectures, such as the U-Net, have emerged as promising alternatives. Originally developed for biomedical image segmentation, the U-Net framework features a symmetric structure with skip connections that directly transfer feature maps from encoder layers to corresponding decoder layers. This design facilitates the preservation of both global context and fine-grained local features during reconstruction, making U- Net particularly well-suited for tasks requiring high spatial accuracy. Recent studies (Bao et al., 2023; Sofos et al., 2025) have begun to explore the application of U-Net-based models to fluid dynamics problems. However, the integration of U-Net architectures into the super-resolution reconstruction of near-wall streaks and wall-bounded coherent structures has been explored less extensively.

In this study, we perform a super-resolution reconstruction of near-wall turbulent structures using two deep learning frameworks: the conventional SRCNN and the U-Net framework. The training data are derived from high-fidelity, wall-resolved large eddy simulations (WRLES) of turbulent channel flow at $Re_\tau =$ 1,000 (Fan et al., 2024), while low-resolution inputs are generated by downsampling with ratios $r = 4$ and $r = 8$. We specially focus on the reconstruction performance in different regions of the turbulent boundary layer: the inner layer ($y^+ = 15$) and the outer layer ($y/\delta = 0.15$). The paper is structured as follows: In the second section, we introduce the flow setup of WRLES, data preparation for ML training, and architecture of the neural network. The third section presents the results and detailed discussion, and the conclusions are drawn in the final section.

METHODOLOGY

Governing Equations

The high-fidelity WRLES of turbulent channel flow is conducted using the open-source computational fluid dynamics platform OpenFOAM. By applying a filter to the incompressible N-S equations, the governing equations for LES can be obtained.

$$\frac{\partial \tilde{u}_i}{\partial x_i} = 0 \tag{1}$$

$$\frac{\partial \tilde{u}_i}{\partial t} + \frac{\partial \tilde{u}_i \tilde{u}_j}{\partial x_j} = -\frac{1}{\rho}\frac{\partial \tilde{p}}{\partial x_i} + \nu \frac{\partial^2 \tilde{u}_i}{\partial x_j \partial x_j} + \frac{\partial \tau_{ij}^{sgs}}{\partial x_j} \tag{2}$$

where $\tilde{u}_i$ $(i = 1, 2, 3)$ is the filtered velocity component in the x_i direction of the flow field; $\tilde{p}$ is the filtered pressure of the flow field; ν is the kinematic viscosity of the fluid; and τ_{ij}^{sgs} is the SGS stress term. τ_{ij}^{sgs} is given by

$$\tau_{ij}^{sgs} = 2\nu_{sgs}\tilde{S}_{ij} + \frac{1}{3}\tau_{kk}^{sgs}\delta_{ij} \tag{3}$$

where $\tilde{S}_{ij}$ is the resolved strain-rate tensor; δ_{ij} is the Kronecker delta; and ν_{sgs} is the SGS eddy viscosity. In this study, the wall-adapting local eddy-viscosity (WALE) model (Nicoud and Ducros, 1999) is applied as

$$\nu_{sgs} = (C_w \Delta)^2 \frac{(S_{ij}^d S_{ij}^d)^{3/2}}{(\tilde{S}_{ij}\tilde{S}_{ij})^{5/2} + (S_{ij}^d S_{ij}^d)^{5/4}} \tag{4}$$

where $C_w = 0.325$ is the WALE coefficient; Δ is the cube root of local cell volume; and S_{ij}^d is the traceless symmetric part of the square of the velocity gradient tensor. The accuracy of the WALE model has been validated extensively in our previous studies (Fan, Chen, et al., 2025; Fan, Zhao, and Wan, 2025).

Flow Setup of High-fidelity Simulation

Figure 1 shows the computational domain of WRLES, and the size is set to $L_x \times L_y \times L_z = 2\pi\delta \times 2\delta \times \pi\delta$, where $\delta = 1$ m is the channel half-height; and x, y, and z denote the streamwise, wall-normal, and spanwise directions, respectively. Periodic boundary conditions are applied in the streamwise and spanwise directions. A no-slip velocity boundary condition and a zero-gradient pressure condition are applied uniformly on both the top and bottom walls. A source term is introduced into the momentum equation to maintain the bulk mean velocity U_b to a constant. The Reynolds numbers based on the bulk velocity and friction velocity are $Re_b = U_b\delta/\nu = 20{,}000$ and $Re_\tau = u_\tau\delta/\nu = 1{,}000$, where $u_\tau = \sqrt{\tau_w/\rho}$ is the friction velocity on the wall.

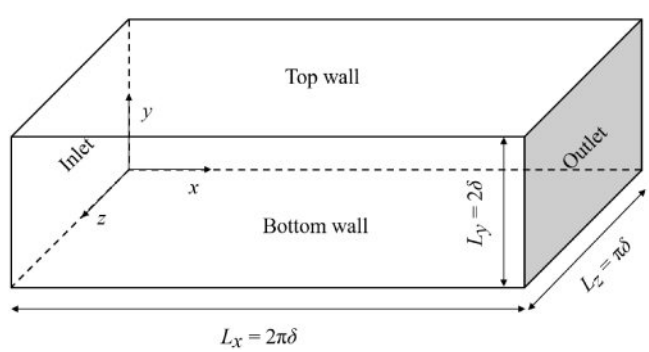

Fig. 1 Computational domain

Case	$N_x \times N_y \times N_z$	Δx^+	Δy^+	Δz^+	Δt^+
WRLES	$321 \times 217 \times 321$	19.6	0.79 ~ 15.0	9.8	0.1

Table 1 Parameters of computational meshes

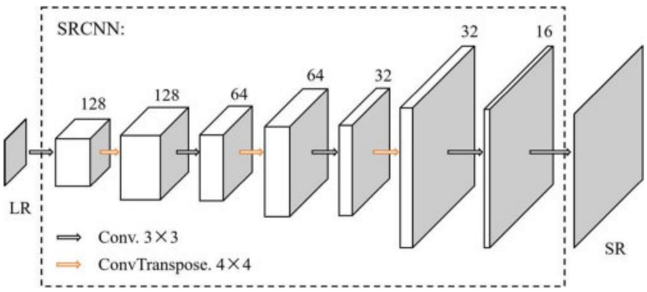

Fig. 2 Architecture of the SRCNN model for $r = 8$

In terms of the computational meshes, the key parameters are demonstrated in Table 1, where $N_x \times N_y \times N_z$ are the numbers of grid points in three directions; N_{total} is the total number of grid points; Δx^+, Δy^+ and Δz^+ are the nondimensional grid spacings; and Δt^+ is the non-dimensional computational time step. In this paper, variables with superscript "+" are nondimensionalized using characteristic length ν/u_τ and characteristic velocity u_τ. The nondimensional cell sizes in the wall-normal direction grow gradually from 0.79 at the wall to 15.0 using a linear stretching ratio of 1.05, after which, it is uniform. The total number of cells is approximately 22.1 million.

In terms of the numerical schemes and solver, the coupled pressure-velocity is solved using the PISO algorithm (Issa, 1986), with three pressure corrections at each time step. In addition, the temporal term employs the second-order implicit backward scheme (Jasak, 1996). The gradient and Laplacian terms are discretized using the second-order linear scheme. Regarding the discretization of the convective term, the second-order central differencing is used for the convection term in the N-S equations.

The simulations are run for 20 flow-past times, with the first 10 flow-past times used for flow development and the remaining 10 flow-past times used for statistical analysis.

Architecture of Neural Network

To investigate the effectiveness of SR methods for turbulent flow fields, we employed two deep learning architectures. As shown in Fig. 2, the first network is the SRCNN architecture, which is consistent with the previous study of Kim et al. (2021). The model takes the low-resolution velocity field as input, and the transposed convolution layers progressively upscale the input data, enabling the model to learn the upsampling process directly from the training data. The architecture alternates between convolutional layers and transposed convolutional layers, with kernel sizes of 3×3 and 4×4, respectively. For different downsampling ratios, the model architecture is slightly adjusted. Owing to its simplicity and low computational cost, SRCNN serves as a baseline model in this study.

Figure 3 shows the super-resolution architecture based on the U-Net framework. It adopts an encoder–decoder structure with symmetric skip connections, enabling efficient fusion of multi-scale spatial information. The encoder path progressively downsamples the input through stacked convolutional and pooling layers, capturing hierarchical features at different scales. The decoder path performs upsampling and combines high-level features with fine-scale details via skip connections from the corresponding encoder layers. In this work, bicubic-interpolated low-resolution fields are used as input to the U-NetSR model.

Input and Output

The input data consists of LR streamwise velocity fields generated by downsampling HR fields at a specific ratio ($r = 4$ and 8). The downsampling process discretizes the HR data, and the LR data are obtained by selecting discrete points from the HR data. For instance, in the case of $r = 8$, one data point is selected for every eight points. For all architectures, the output is the reconstructed SR flow field, matching the resolution of the original HR

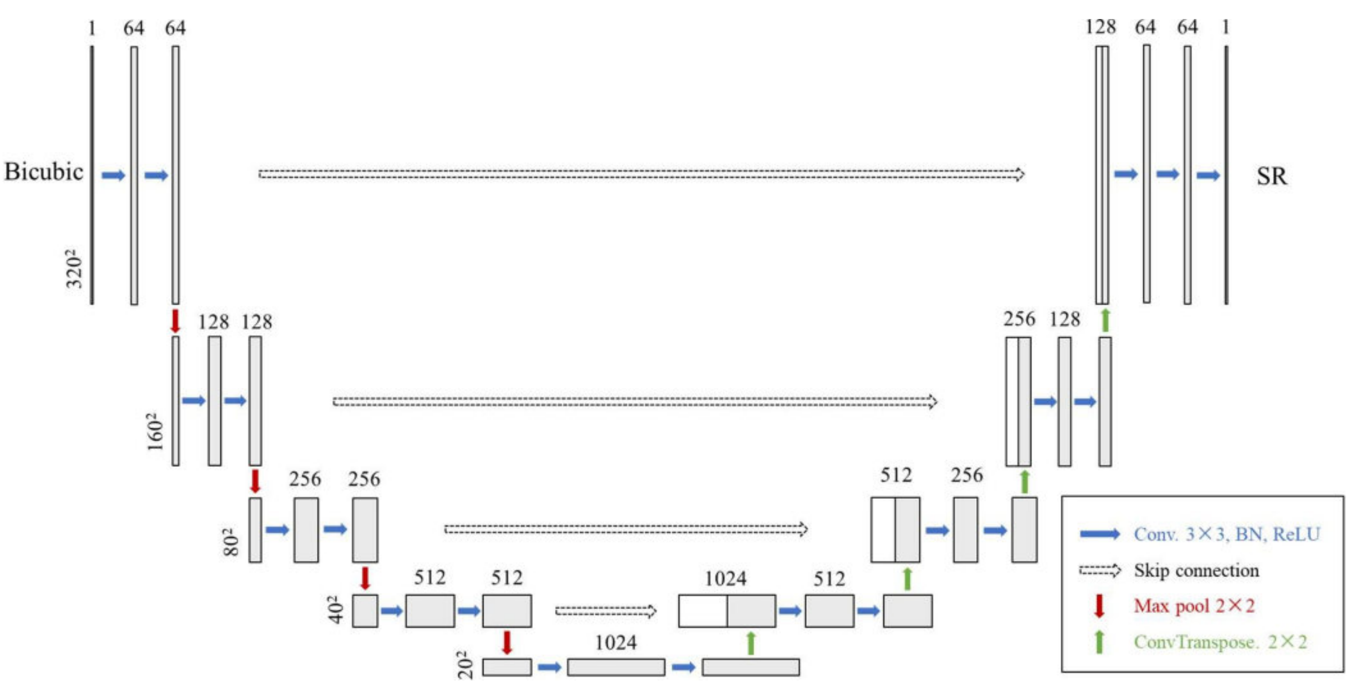

Fig. 3 Architecture of U-NetSR model

data (320 × 320). A total of 1,000 instantaneous flow-field snapshots are extracted from the WRLES database. Among them, 800 snapshots are randomly selected for training, while the remaining 200 snapshots are used as the test dataset for evaluating the performance of both SRCNN and U-NetSR. During training, the models were optimized using the mean squared error (MSE) loss function, which quantifies the pixel-wise difference between the reconstructed SR image and the ground truth HR data. The Adam optimizer was employed with an initial learning rate of 5×10^{-4}, and we reduced it by 1/5 when the loss in validation dataset did not decrease.

RESULTS AND DISCUSSION

This section presents and analyzes the performance of two deep learning models, SRCNN and U-NetSR, in the super-resolution reconstruction of turbulent channel flow at $Re_\tau = 1{,}000$. The evaluation focuses on the reconstruction accuracy of streamwise velocity fields at two representative wall-normal locations: the inner layer ($y^+ = 15$) and the outer layer ($y/\delta = 0.15$), under two downsampling ratios ($r = 4$ and 8). Comparisons are made against bicubic interpolation and high-resolution reference data obtained from WRLES. Both qualitative and quantitative analyses are conducted to assess the models' ability to recover small-scale structures and high-frequency information in different regions of the turbulent boundary layer. Special attention is given to the effects of downsampling severity and wall-normal location on model performance.

Validation of Training Data

Figure 4 shows the instantaneous near-wall vortical structures visualized by the Q-criterion. Due to the approximate symmetry of the channel flow, only the vortex structures from the bottom wall to the center of the channel are presented here. As the distance from the wall increases, the size of the vortices also increases. The multi-scale phenomena of wall-bounded turbulent flow is easily observed.

Figure 5 shows the instantaneous contours of streamwise velocity fields at $y^+ \approx 15$ and $y/\delta = 0.15$. The near-wall flow field is organized into streaky quasi-streamwise structures composed of high-speed and low-speed flows. These flows are elongated in the streamwise direction and alternately arranged in the spanwise direction. The low-speed flow primarily originates from the ejection effect, while the high-speed flow results from the sweeping effect of large-scale vortices from above. Compared to the velocity streak structures at $y^+ = 15$, the flow at $y/\delta = 0.15$ is dominated by meandering large-scale structures.

Figure 6 shows the mean streamwise velocity profile and the resolved Reynolds stresses in inner scaling, which are compared

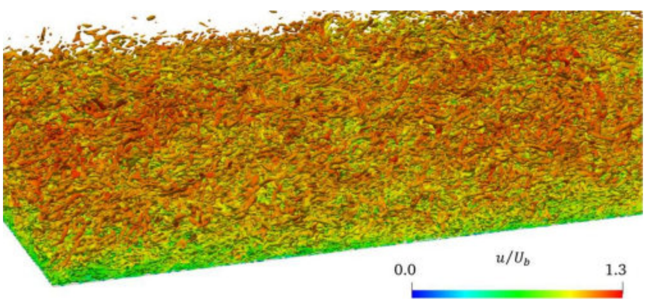

Fig. 4 Instantaneous near-wall vortical structures visualized by the Q-criterion ($Q = 0.05$)

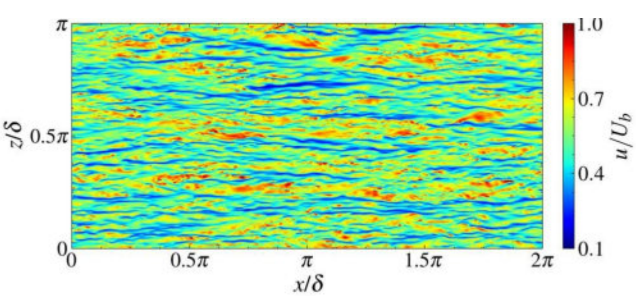

(a) Inner layer: $y^+ \approx 15$

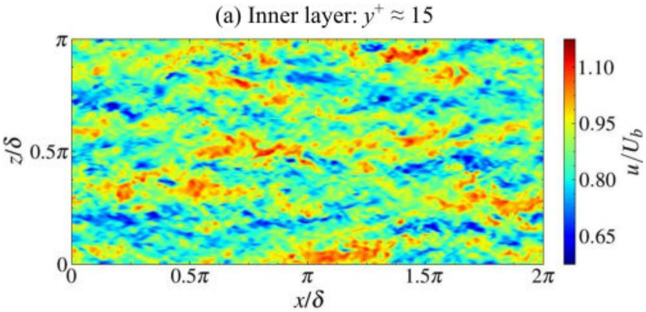

(b) Outer layer: $y/\delta = 0.15$

Fig. 5 Instantaneous contours of streamwise velocity fields at different wall-normal positions

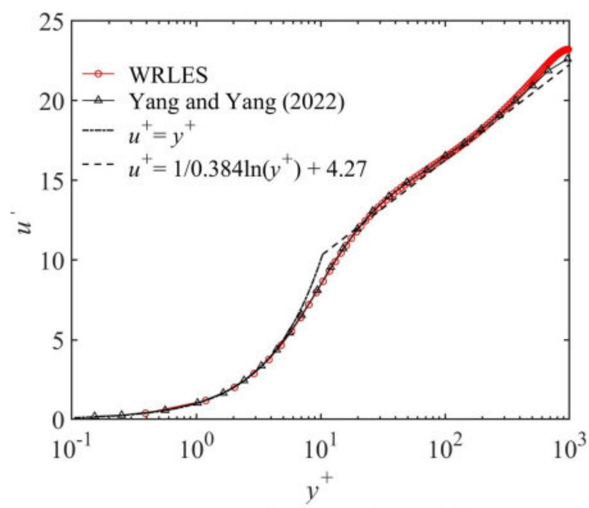

(a) Streamwise velocity profiles

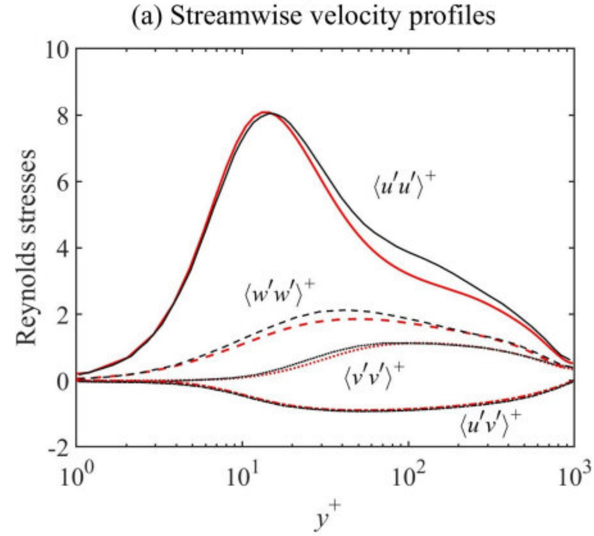

(b) Inner-scaled Reynolds stresses

Fig. 6 Validation of present WRLES (red line represents results of WRLES; black line shows DNS data)

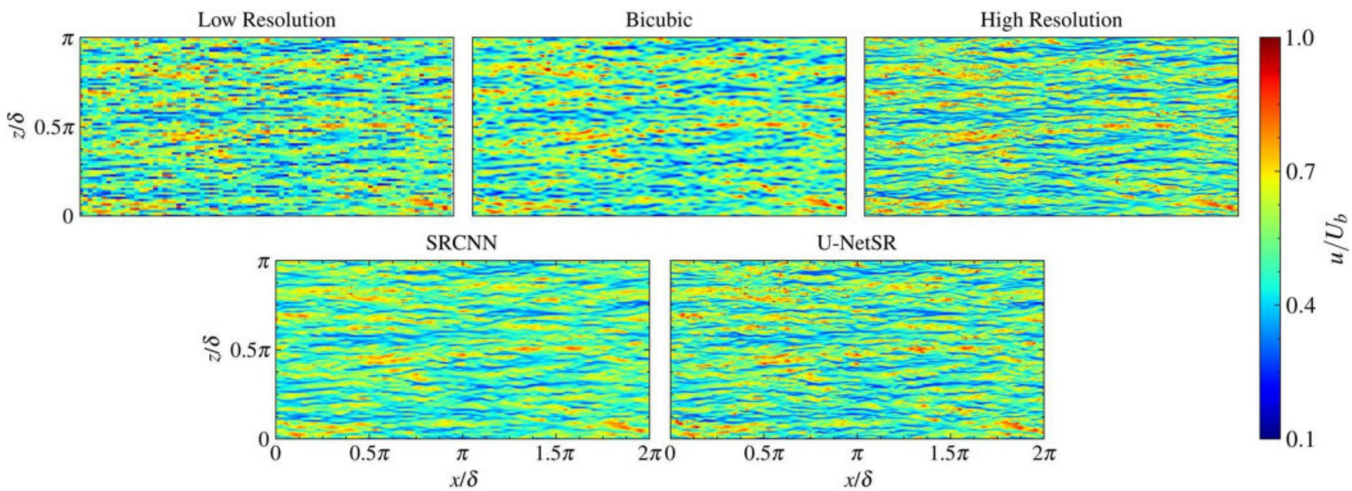

Fig. 7 Reconstructed inner-layer velocity fields ($y^+ \approx 15$) using different neural networks at $r = 4$

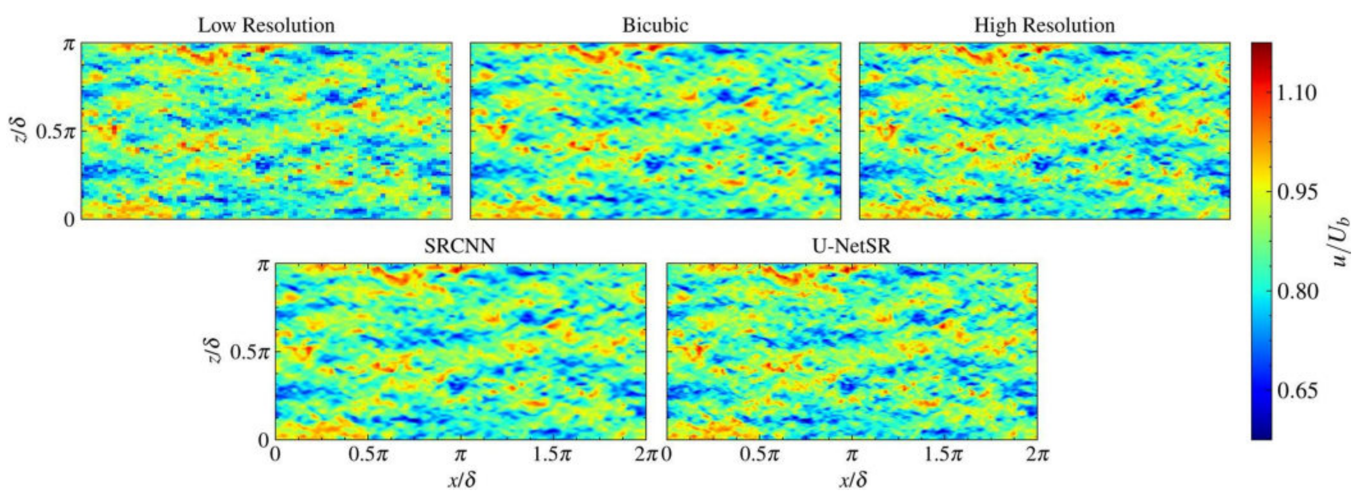

Fig. 8 Reconstructed outer-layer velocity fields ($y/\delta = 0.15$) using different neural networks at $r = 4$

with the DNS data (Yang and Yang, 2022). The results of WRLES match well with empirical formulas in both the viscous sublayer and logarithmic layer. For the Reynolds stress $\langle uu \rangle^+$, a peak of Reynolds stress is observed at $y^+ = 15$. The agreement between the DNS data and the present WRLES is satisfactory. Considering that $y^+ = 15$ corresponds to the location of the near-wall turbulent kinetic energy peak, where turbulent motions are most active, we performed super-resolution reconstruction on the streamwise velocity field at $y^+ = 15$.

Results for Downsampling Ratio $r = 4$

In this subsection, we first evaluate the super-resolution reconstruction performance of SRCNN and U-NetSR models under a moderate downsampling ratio of $r = 4$. The input low-resolution fields are generated by uniformly subsampling the high-resolution WRLES data by a factor of four in each spatial direction. Figures 7 and 8 present the reconstructed instantaneous streamwise velocity fields at two representative wall-normal locations: the inner layer ($y^+ \approx 15$) and the outer layer ($y/\delta = 0.15$). Each figure includes the low-resolution input, bicubic interpolation, SRCNN, U-NetSR, and the high-resolution reference from WRLES for comparison. All velocity fields are plotted using the same color scale to facilitate qualitative assessment.

Figure 7 shows the reconstructed inner-layer velocity field at $y^+ \approx 15$, where elongated low- and high-speed streaks dominate the near-wall region. In the low-resolution input, most of these streaks are obscured due to the coarse spatial resolution, with the field appearing heavily pixelated and lacking coherent structure. Bicubic interpolation produces a smoother result but fails to recover the thin, alternating streaks evident in the high-resolution reference. The result from SRCNN exhibits noticeable improvement, with the main streak orientation and spacing partially restored. The reconstructed field is generally smooth, with slightly attenuated high-frequency details, yet it retains the basic structure of the wall-parallel streaks. While some of the weaker modulations are missing, the overall streak pattern becomes clearly visible. In contrast, the U-NetSR model reconstructs the near-wall velocity field with high fidelity, recovering streak alignment and intensity close to the WRLES reference. The streak boundaries are sharper, and small-scale variations are more accurately reproduced, indicating that U- NetSR captures a broader range of turbulent scales and better preserves near-wall structural details.

Figure 8 illustrates the reconstruction results at $y/\delta = 0.15$, corresponding to the outer region of the boundary layer. While the low-resolution input and bicubic interpolation lack sufficient detail to represent small-scale eddies, the SRCNN model provides a modest improvement. Compared to bicubic, the reconstructed field from SRCNN appears smoother and more structured, with several medium-sized features partially recovered. However, the improvement remains limited, and many localized fluctuations present in the high-resolution field are still not well captured. The

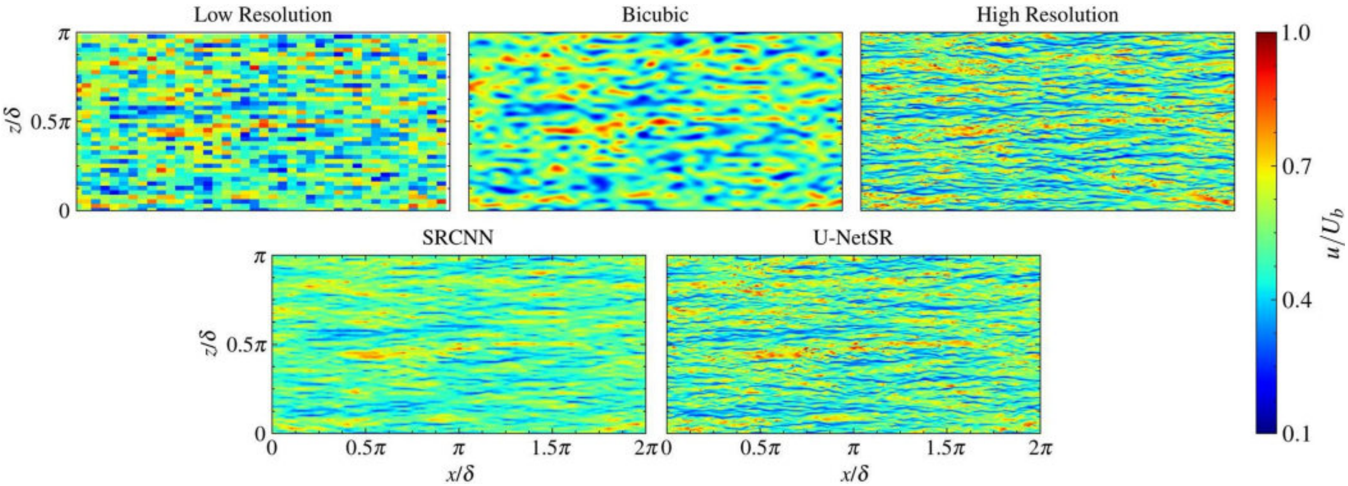

Fig. 9 Reconstructed inner-layer velocity fields ($y^+ \approx 15$) using different neural networks at $r = 8$

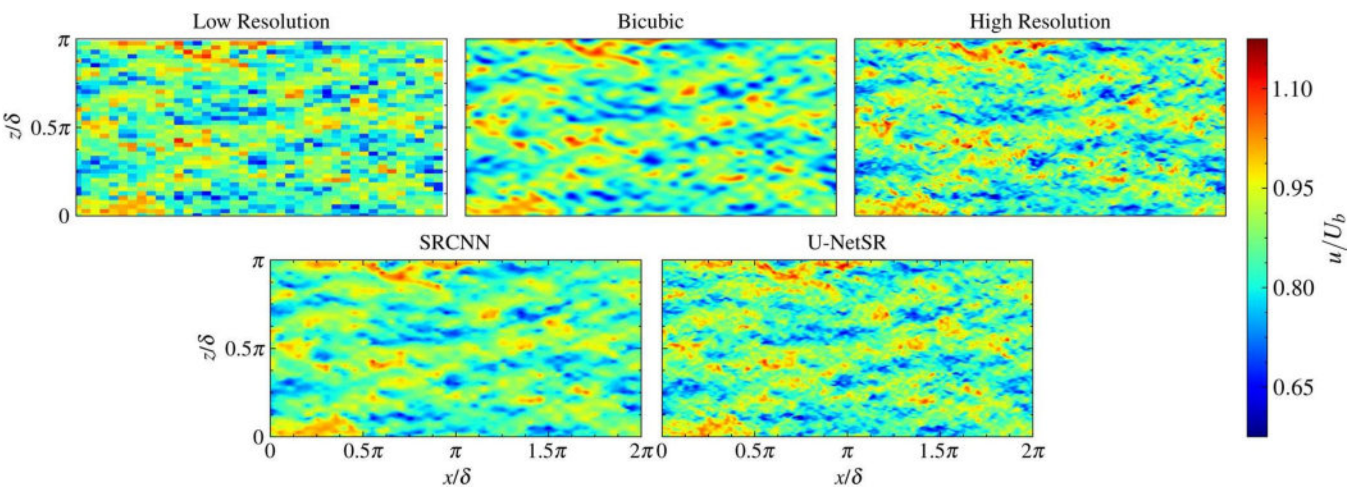

Fig. 10 Reconstructed outer-layer velocity fields ($y/\delta = 0.15$) using different neural networks at $r = 8$

U-NetSR result again demonstrates superior performance, closely replicating the intricate structure and fine-scale variability of the high-resolution field. Small eddies and streak fragments that are missing in the SRCNN output become visible in the U-NetSR reconstruction, and the contrast between adjacent structures is substantially sharper. Overall, for a moderate downsampling ratio, U-NetSR consistently outperforms both bicubic interpolation and SRCNN across both wall-normal regions.

Results for Downsampling Ratio $r = 8$

To further evaluate model robustness under more challenging conditions, we investigate the reconstruction performance at a higher downsampling ratio of $r = 8$, where the input resolution is severely degraded. Figures 9 and 10 display the reconstructed streamwise velocity fields at $y^+ \approx 15$ and $y/\delta = 0.15$, respectively. This scenario represents an extreme case in which most of the small-scale turbulent structures are lost in the low-resolution input, thereby testing the limits of model generalization and learning capacity.

Figure 9 shows the reconstruction results for the near-wall region at $y^+ \approx 15$. The low-resolution input contains almost no recognizable streak features—most spatial variations are heavily aliased or entirely lost. Bicubic interpolation produces a visually smoother result but remains devoid of meaningful small-scale content. The SRCNN reconstruction exhibits a partial recovery of wall-parallel structures; streak alignment can be observed to some degree, suggesting that the model is able to learn and infer low-frequency components of the flow. However, the SRCNN output suffers from excessive smoothing, and the overall structure appears overly diffused. Many of the finer streaks and rapid transitions in velocity are completely suppressed, leading to a blurry appearance. In contrast, the U-NetSR result demonstrates a substantial improvement. The reconstructed field displays well-defined streaks, sharper velocity gradients, and noticeable small-scale modulations. Although the U-NetSR result is still slightly smoother than the high-resolution reference due to the extreme input degradation, it retains a much larger portion of the wall-parallel coherence and finer structure than SRCNN or bicubic interpolation. This result confirms that U-NetSR is capable of learning multiscale spatial features and generalizing even under severe resolution constraints.

Figure 10 shows the outer-layer reconstruction at $y/\delta = 0.15$. The upsampled low-resolution and bicubic fields appear overly smooth and devoid of any small-scale structures. The SRCNN result introduces limited improvement, with a few broad eddy-like patterns reemerging, but the lack of sharpness and spatial complexity is evident. The field remains dominated by large, diffuse velocity regions, and small eddies are almost entirely absent. In contrast, the U-NetSR reconstruction captures a noticeably richer spatial texture. A wide range of eddy sizes is recovered, including small-scale features that align with those seen in the high-resolution reference. The boundaries between high- and low-speed regions are sharper and more clearly delineated, and localized

Case	Bicubic (dB)	SRCNN (dB)	U-NetSR (dB)
$r=4,\ y^+ \approx 15$	32.15	34.93	36.48
$r=4,\ y/\delta=0.15$	41.06	44.48	46.36
$r=8,\ y^+ \approx 15$	29.95	31.74	33.59
$r=8,\ y/\delta=0.15$	37.47	40.03	42.13

Table 2 Peak signal-to-noise ratio of bicubic and two neural networks

fluctuations are visible throughout the field. The improved spatial fidelity in the U-NetSR result demonstrates its advantage in recovering fine-scale outer-layer structures, even when the available input information is extremely limited.

In summary, while all methods experience a degradation in performance at $r=8$, the U-NetSR model consistently delivers the best reconstruction quality. Its ability to recover coherent structures and small-scale turbulence is evident in both the near-wall and outer-layer regions. By contrast, SRCNN is hindered by oversmoothing effects at this high downsampling ratio, and bicubic interpolation remains inadequate. These observations underscore the robustness and superior generalization capability of the U-Net-based architecture for super-resolution reconstruction of wall-bounded turbulence under extreme spatial degradation. The combination of deep hierarchical representation and skip connections likely contributes to its strong generalization capability.

To complement the qualitative assessment, Table 2 presents the peak signal-to-noise ratio (PSNR) for all reconstruction cases using bicubic interpolation, SRCNN, and U-NetSR. PSNR is a widely used image fidelity metric that quantifies the similarity between the predicted and reference high-resolution fields, with higher values indicating better reconstruction accuracy. The definition of PSNR is given as:

$$\mathrm{PSNR} = 10 \cdot \log_{10}\left(\frac{\mathrm{MAX}_\mathrm{I}^2}{\mathrm{MSE}}\right) = 20 \cdot \log_{10}\left(\frac{\mathrm{MAX}_\mathrm{I}}{\sqrt{\mathrm{MSE}}}\right) \tag{5}$$

where MAX_I represents the maximum pixel value of the image, and the unit of PSNR is dB. These PSNR results quantitatively confirm the visual observations in Figs. 7–10.

Across all test cases, U-NetSR consistently achieves the highest PSNR values, demonstrating its superior capability in restoring the fine-scale details of the velocity field. For the moderate downsampling ratio ($r=4$), the improvement of U-NetSR over bicubic interpolation is significant, particularly in the outer-layer case ($y/\delta=0.15$), where the PSNR increases from 41.06 dB to 46.36 dB. Even in the inner-layer region ($y^+ \approx 15$), which is more challenging due to the presence of complex near-wall streaks, U-NetSR yields a PSNR of 36.48 dB, outperforming both SRCNN (34.93 dB) and bicubic (32.15 dB).

Under the more challenging condition of $r=8$, all models experience a decline in PSNR due to the severe resolution loss. Nevertheless, U-NetSR remains the top performer, achieving 33.59 dB at $y^+ \approx 15$ and 42.13 dB at $y/\delta=0.15$. Notably, the performance drop for U-NetSR is less drastic compared to that for SRCNN and bicubic, highlighting its robustness to extreme downsampling. SRCNN also consistently improves upon bicubic, though the gap between SRCNN and U-NetSR becomes more pronounced as the downsampling ratio increases.

CONCLUSIONS

This study investigates the application of deep learning techniques for the super-resolution reconstruction of near-wall turbulent structures in channel flow at $Re_\tau = 1{,}000$, using wall-resolved LES data as ground truth. Two convolutional neural network models, SRCNN and a U-Net-based architecture (U-NetSR), are evaluated and compared against bicubic interpolation under two levels of downsampling ($r=4$ and $r=8$), focusing on both the inner-layer ($y^+ \approx 15$) and outer-layer ($y/\delta=0.15$) regions of the turbulent boundary layer.

The results demonstrate that both neural network models outperform bicubic interpolation in recovering fine-scale structures from low-resolution inputs. While SRCNN provides a modest improvement in flow reconstruction, particularly at moderate downsampling, it suffers from oversmoothing at higher downsampling ratios. In contrast, U-NetSR consistently delivers high-fidelity reconstructions across all test cases. It effectively captures elongated streaks and small-scale turbulent fluctuations, even in the highly degraded input scenario ($r=8$). Quantitative evaluation using PSNR further confirms the superior performance of U-NetSR, with improvements up to 4–5 dB over bicubic and 2–3 dB over SRCNN.

It is worth noting that the WRLES used to generate the training dataset consumes over 40,000 core-hours, while the trained U-NetSR model can reconstruct a high-resolution snapshot within only a few seconds, highlighting its significant computational advantage.

These findings highlight the strong potential of U-Net-based architectures for enhancing the resolution of turbulent flow fields while significantly reducing the cost of high-fidelity simulations. The demonstrated robustness of U-NetSR across different wall-normal regions and sampling levels suggests its applicability in accelerating data acquisition, enabling efficient storage, and supporting high-resolution flow field reconstruction in complex wall-bounded turbulence scenarios.

ACKNOWLEDGEMENTS

This work is supported by the National Natural Science Foundation of China (52131102), to which the authors are most grateful.

REFERENCES

Bao, K, Zhang, XY, Peng, W, and Yao, W (2023). “Deep Learning Method for Super-Resolution Reconstruction of the Spatio-Temporal Flow Field,” *Adv Aerodyn*, 5(1), 19. https://doi.org/10.1186/s42774-023-00148-y.

Deng, ZW, He, CX, Liu, YZ, and Kim, KC (2019). “Super-Resolution Reconstruction of Turbulent Velocity Fields Using a Generative Adversarial Network-Based Artificial Intelligence Framework,” *Phys Fluids*, 31(12), 125111. https://doi.org/10.1063/1.5127031.

Dong, C, Loy, CC, He, K, and Tang, X (2016). “Image Super-Resolution Using Deep Convolutional Networks,” *IEEE Trans Pattern Anal Mach Intell*, 38(2), 295–307. https://doi.org/10.1109/TPAMI.2015.2439281.

Fan, GQ, Chen, H, Zhao, WW, and Wan, DC (2025). “Scaling Laws and Space–Time Characteristics of Wall Pressure Fluctuations in an Axisymmetric Boundary Layer with Varying Pressure Gradient,” *J Fluid Mech*, 1016, A28. https://doi.org.10.1017/jfm.2025.10427.

Fan, GQ, Zhao, WW, and Wan, DC (2025). “Near-Wall Turbulent Fluctuations and Coherent Structures in Wall-Modeled Large-Eddy Simulation,” *Phys Fluids*, 37(9), 95108. https://doi.org/10.1063/5.0282005.

Fan, GQ, Zhu, J, Zhao, WW, and Wan, DC (2024). "A Comparative Study between Wall-Resolved and Wall-Modeled Large Eddy Simulation of Turbulent Channel Flows," *Proc 34th Int Ocean Polar Eng Conf*, Rhodes, Greece, ISOPE, 220–226.

Fukami, K, Fukagata, K, and Taira, K (2019). "Super-Resolution Reconstruction of Turbulent Flows with Machine Learning," *J Fluid Mech*, 870, 106–120. https://doi.org.10.1017/jfm.2019.238.

Fukami, K, Fukagata, K, and Taira, K (2021). "Machine-Learning-Based Spatio-Temporal Super Resolution Reconstruction of Turbulent Flows," *J Fluid Mech*, 909, A9. https://doi.org.10.1017/jfm.2020.948.

Issa, RI (1986). "Solution of the Implicitly Discretised Fluid Flow Equations by Operator-Splitting," *J Comput Phys*, 62(1), 40–65. https://doi.org/10.1016/0021-9991(86)90099-9.

Jasak, H (1996). *Error Analysis and Estimation for the Finite Volume Method with Applications to Fluid Flows*, PhD thesis, Imperial College, University of London, UK.

Kim, H, Kim, J, Won, S, and Lee, C (2021). "Unsupervised Deep Learning for Super-Resolution Reconstruction of Turbulence," *J Fluid Mech*, 910, A29. https://doi.org.10.1017/jfm.2020.1028.

Nicoud, F, and Ducros, F (1999). "Subgrid-Scale Stress Modelling Based on the Square of the Velocity Gradient Tensor," *Flow Turbul Combust*, 62, 183–200. https://doi.org/10.1023/A:1009995426001.

Nista, L, et al. (2024). "Influence of Adversarial Training on Super-Resolution Turbulence Reconstruction," *Phys Rev Fluids*, 9(6), 064601. https://doi.org/10.1103/PhysRevFluids.9.064601.

Sofos, F, Drikakis, D, Kokkinakis, IW, and Spottswood, SM (2025). "Spatiotemporal Super-Resolution Forecasting of High-Speed Turbulent Flows," *Phys Fluids*, 37(1), 016124. https://doi.org/10.1063/5.0250509.

Wu, HK, et al. (2024). "High-Flexibility Reconstruction of Small-Scale Motions in Wall Turbulence Using a Generalized Zero-Shot Learning," *J Fluid Mech*, 990, R1. https://doi.org.10.1017/jfm.2024.521.

Xu, Q, Zhuang, Z, Pan, Y, and Wen, B (2023). "Super-Resolution Reconstruction of Turbulent Flows with a Transformer-Based Deep Learning Framework," *Phys Fluids*, 35(5), 055130. https://doi.org.10.1063/5.0149551.

Yang, BW, and Yang, ZX (2022). "On the Wavenumber-Frequency Spectrum of the Wall Pressure Fluctuations in Turbulent Channel Flow," *J Fluid Mech*, 937, A39. https://doi.org/10.1017/jfm.2022.137.

Zeng, K, Zhang, Y, Xu, H, and Feng, XL (2024). "Super-Resolution Reconstruction of Turbulent Flows with a Hybrid Framework of Attention," *Phys Fluids*, 36(6), 065107. https://doi.org/10.1063/5.0203869.

Zhou, ZD, Li, BL, Yang, XL, and Yang, ZX (2022). "A Robust Super-Resolution Reconstruction Model of Turbulent Flow Data Based on Deep Learning," *Comput Fluids*, 239, 105382. https://doi.org/10.1016/j.compfluid.2022.105382.